

A Trilayer Structure with Surface Binary Microsphere Array for Radiative Cooling and Heating Regulation

Tong Wang,^{a,b,†} Shuqi Zhang,^{a,b,†} Qian Zhu,^{a,b} Jie Zhang,^{a,b} Yu Zhang,^c Yanping Du,^d Limin Wu,^c Min Gu,^{a,b,*} Yinan Zhang^{a,b,*}

^aSchool of Artificial Intelligence Science and Technology, University of Shanghai for Science and Technology, Shanghai 200093, China.

^bInstitute of Photonic Chips, University of Shanghai for Science and Technology, Shanghai 200093, China.

^cDepartment of Materials Science and State Key Laboratory of Molecular Engineering of Polymers, Fudan University, Shanghai 200433, China.

^dSchool of Engineering, Lancaster University, Lancaster LA1 4YW, UK

*Corresponding author. Email: zhangyinan@usst.edu.cn (Y.Z), gumin@usst.edu.cn (M.Gu)

[†]These authors contributed equally to this work.

ABSTRACT

Passive daytime radiative cooling is of tremendous interest but would be overcooling during cold nights or winter days, exacerbating the heating cost, especially in high-latitude areas. Integrating the heating and cooling in one photothermal system can avoid the cooling penalties and potential barriers for wide practical scenarios. Herein, we demonstrate a trilayer structure with visible and infrared spectral engineering for all-season radiative cooling and heating. The cooling mode with a solar reflectivity of 0.95 and a mid-infrared emissivity of 0.98 endows a comparable daytime subambient cooling of 9.8 °C with a theoretically net cooling power of 76.6 W/m². Meanwhile, the heating mode with a solar absorptivity of 0.88 and a mid-infrared emissivity of 0.28 yields a daytime above-ambient heating of 16.3 °C with a theoretically net heating power of 667.8 W/m². Promisingly, the surface binary microsphere array further enhances the mid-infrared emissivity, superhydrophobicity, and environmental durability, making the trilayer structure a viable pathway for thermal management with great potential in electricity savings and CO₂ emission reduction. This work offers new possibilities in designing next-generation radiative cooling materials, greatly widening the scope of use.

KEYWORDS

radiative cooling; trilayer structure; binary microsphere array; solar heating; energy-saving

INTRODUCTION

Global energy requirements are rising owing to the increase in concerns associated with global warming and rapid depletion of energy resources. Particularly, heating and cooling systems account for approximately 40% of energy consumption in commercial and residential construction.¹⁻³ It is predicted that the heating and cooling energy use is still expected to strongly grow until the middle of the century, with an approximately 84% and 79% projected increase by 2050 as compared to 2010.⁴ Developing high-efficiency and cost-effective passive thermal management toward sustainable carbon neutrality has been recognized as an indispensable and urgent task. To this end, harvesting energy from the sun and outer space plays ubiquitous roles throughout the long history of human civilization.^{5, 6} Recently, passive daytime radiative cooling (PDRC) has been of tremendous interest and could address critical sustainability issues by reflecting sunlight ($\lambda \sim 0.3\text{-}2.5 \mu\text{m}$) and shedding heat flow back to outer space as infrared radiation through the atmospheric transparency window ($\lambda \sim 8\text{-}13 \mu\text{m}$).⁷

10

Current seminal and high-profile PDRC designs, such as nanophotonic structures,¹¹⁻¹⁵ metamaterials,¹⁶⁻¹⁹ porous structural materials,²⁰⁻²⁶ polymer-coated metal films,²⁷⁻²⁹ bioinspired structural materials,³⁰⁻³² and white cool-roof paints,³³⁻³⁵ offer an alternative pathway to electrical cooling in the hot daytime, but are overcooling during cold nights or winter days and exacerbate the heating cost, especially in high-latitude areas.^{36, 37} It would be desirable to integrate heating and cooling in one photothermal regulation system to avoid cooling penalties and potential barriers for wide practical scenarios.^{38, 39} Dynamic radiative thermoregulation is now emerging as a frontier in renewable energy research because it can achieve on-demand

switching between radiative cooling and heating modes in such a quite variable environment. Efforts toward these integrated systems have focused on active on-demand and passive adaptive manners based on their driving force of mode switching. The passive adaptive system is typically triggered by ambient temperature or humidity variation, but its implementation has been largely limited to visible and near-infrared wavelength regimes,^{36, 40-43} such as the poly(N-isopropylacrylamide) (PNIPAm) hydrogel and thermochromic chameleon microcapsules we reported previously.^{37, 44} Active on-demand tuning system, such as mechanical and electrochromic methods, enables a synergistic and programmable radiative regulation in a substantially wide bandwidth from ultraviolet (UV, ~ 300 nm in wavelength) to mid-infrared (MIR, ~25 μm for ambient thermal radiation or ~14 μm for atmospheric window) and is more favorable in real applications.⁴⁵⁻⁴⁸ Conceptually, as shown in **Figures 1a-b**, the ideal radiative cooling with a solar absorptivity (0.3-2.5 μm) of 0 (solar reflectivity of 1.0) and MIR emissivity (2.5-25 μm) of 1.0 in hot weather is desirable. On the contrary, ideal radiative heating is expected to have a solar absorptivity of 1.0 (solar reflectivity of 0) and MIR emissivity of 0 to suppress enormous heat dissipation *via* thermal re-radiation in cold outside environments, showing exactly opposite requirement for cooling and heating modes.

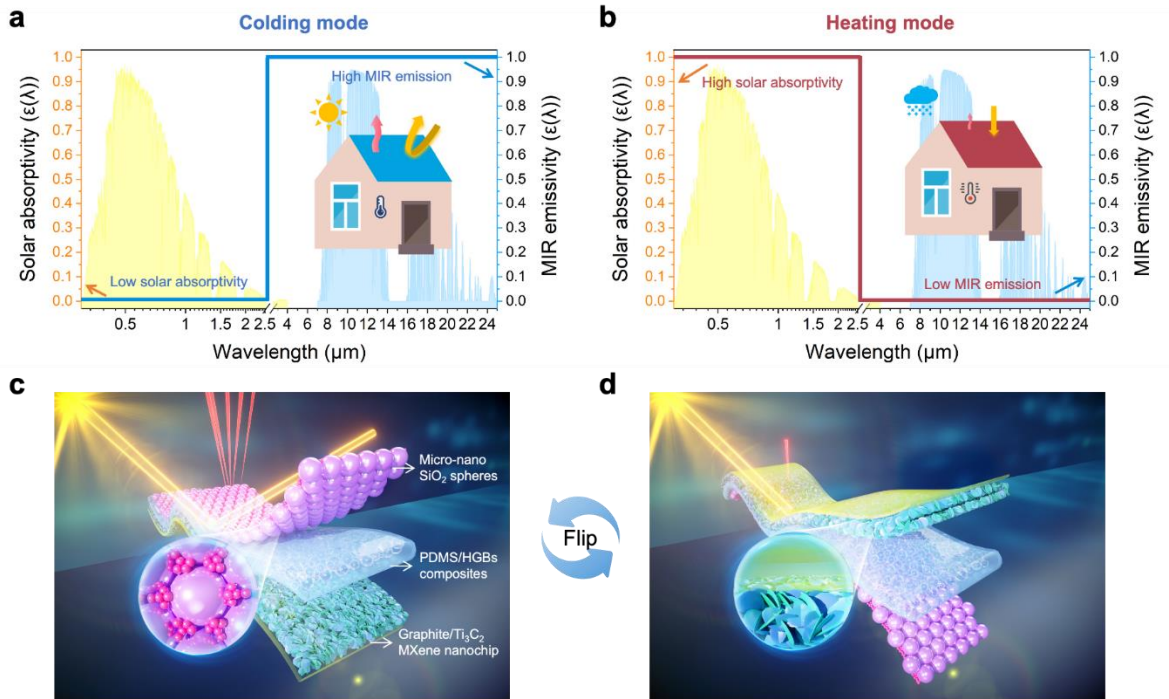


Figure 1. Conceptual design of the trilayer structure for all-season radiative thermoregulation. (a,b) Ideal solar absorptivity and MIR emissivity spectra of the trilayer structure, having exactly opposite requirement for cooling and heating modes. (c,d) Schematic of trilayer structure in cooling mode and heating mode, showing high solar reflectance and high MIR thermal emittance in cooling mode, and low solar reflectance and low MIR thermal emittance in heating mode.

In this work, we demonstrate a trilayer structure with visible and infrared spectral engineering for all-season radiative thermoregulation. As shown in Figures 1c and d, the top-layer consists of hexagonally close-packed SiO_2 microspheres embedded with a couple of nanoscale SiO_2 spheres in each interstice. The interlayer is polydimethylsiloxane/hollow glass beads (PDMS/HGBs) hybrid film and the underlayer is composed of uniformly distributed graphite sheet and Ti_3C_2 MXene nanochip (G/MXene). Specifically, the surface binary microsphere array top-layer and PDMS/HGBs interlayer synergistically reflect sunlight to minimize the solar heat gain and radiate MIR light through the atmospheric transparency window to harvest the coldness of the universe. Once the ambient temperature exceeds a certain

threshold, the flipped asymmetric structured film with G/MXene surface as top-layer achieves high solar absorptivity and restrained MIR emissivity to maximize radiative heating power. Promisingly, this trilayer structure provides high solar reflectivity ($R_{\text{solar}} = 0.95$) and strong emissivity across the atmospheric transparency window ($E_{8-13\mu\text{m}} = 0.98$) in cooling mode, endowing a comparable daytime subambient cooling of 9.8°C in rooftop test on a typical clear sunny day in Shanghai, China, and a theoretical net cooling power of 76.6 W/m^2 under 800 W/m^2 of solar irradiance. Likewise, the trilayer structure realizes a solar absorptivity (A_{solar}) of 0.88 and an $E_{8-13\mu\text{m}}$ of 0.28 in heating mode, which manifests a daytime above-ambient heating of 16.3°C with a theoretical net heating power of 667.8 W/m^2 . Importantly, the surface binary microsphere array consisting of the SiO_2 microsphere and SiO_2 nanospheres synergistically facilitates the MIR emissivity enhancement and the surface wettability transformation from Wenzel state to Cassie-Baxter state with a water contact angle (WCA) of 156° . Here we define the solar spectrum regulation amplitude as $\eta_R = R_{\text{solar-cooling}}/R_{\text{solar-heating}} = 0.95/0.12=7.92$ and the mid-infrared spectrum regulation amplitude as $\eta_E = E_{8-13\mu\text{m-cooling}}/E_{8-13\mu\text{m-heating}} = 0.98/0.28=3.5$. These above values are on par with or exceeds those in previous reports (Table S1) and result in superb on-demand radiative thermoregulation capability, high adaption to a dynamic external environment exemplified by an average temperature difference ($\Delta T_{\text{cooling-heating}}$) of 26.1°C , and robustly superhydrophobic, self-cleaning and aging-resistant performance. For residential building applications in ten cities representing different dividing regions of the world, our trilayer structure yields up to 12.04% and 6.67% of annual cooling and heating energy saving, respectively, compared with commercially available white paint,

which has a significant advantage over single-cooling and single-heating modes in electricity savings and global CO₂ emission reduction.

RESULTS AND DISCUSSION

Morphology and Spectroscopic Response of the Trilayer Structure. Our trilayer structure achieves a scale-up and cost-effective manufacturing strategy and presents a matte ultrawhite appearance on cooling side and a black appearance on heating side (**Figure 2a**). Notably, for the binary microsphere top-layer, the 700 nm SiO₂ nanospheres are predominantly assembled in each interstice between a monolayer of hexagonally close-packed 5 μm SiO₂ microspheres (m-SiO₂) array, presenting a well-defined, rough and micro-and nanoscale SiO₂ (m/n-SiO₂) surface (Figures 2b-d and S1). For the PDMS/HGBs interlayer, we can see the spherical morphology and hollow HGBs with a broad size distribution of 5-15 μm are randomly embedded in PDMS matrix (Figures 2e and S2). For the G/MXene underlayer, it can be observed that an ultrathin uniformly distributed Ti₃C₂ MXene nanochip layer (less than 2 μm thickness) is coated on a 15-μm-thick graphite layer, collectively serving as a heating function side (Figure 2f). Figures 2g-h demonstrate the solar absorptivity and MIR emissivity of the trilayer structure with a thickness of ~ 800 μm. Exhilaratingly, the cooling side displays a fairly low average solar absorptivity ($A_{\text{solar}} = 0.05$) and high average thermal emissivity over a broad bandwidth ($E_{8-13\mu\text{m}} = 0.98$), which ensures minimum sunlight heat gain and maximum emission of heat to the cold sink of outer space. In contrast, the G/MXene heating side exhibits an A_{solar} of 0.88 and an $E_{8-13\mu\text{m}}$ of 0.28, respectively, allowing for grabbing lots of sunlight and suppressing heat loss.

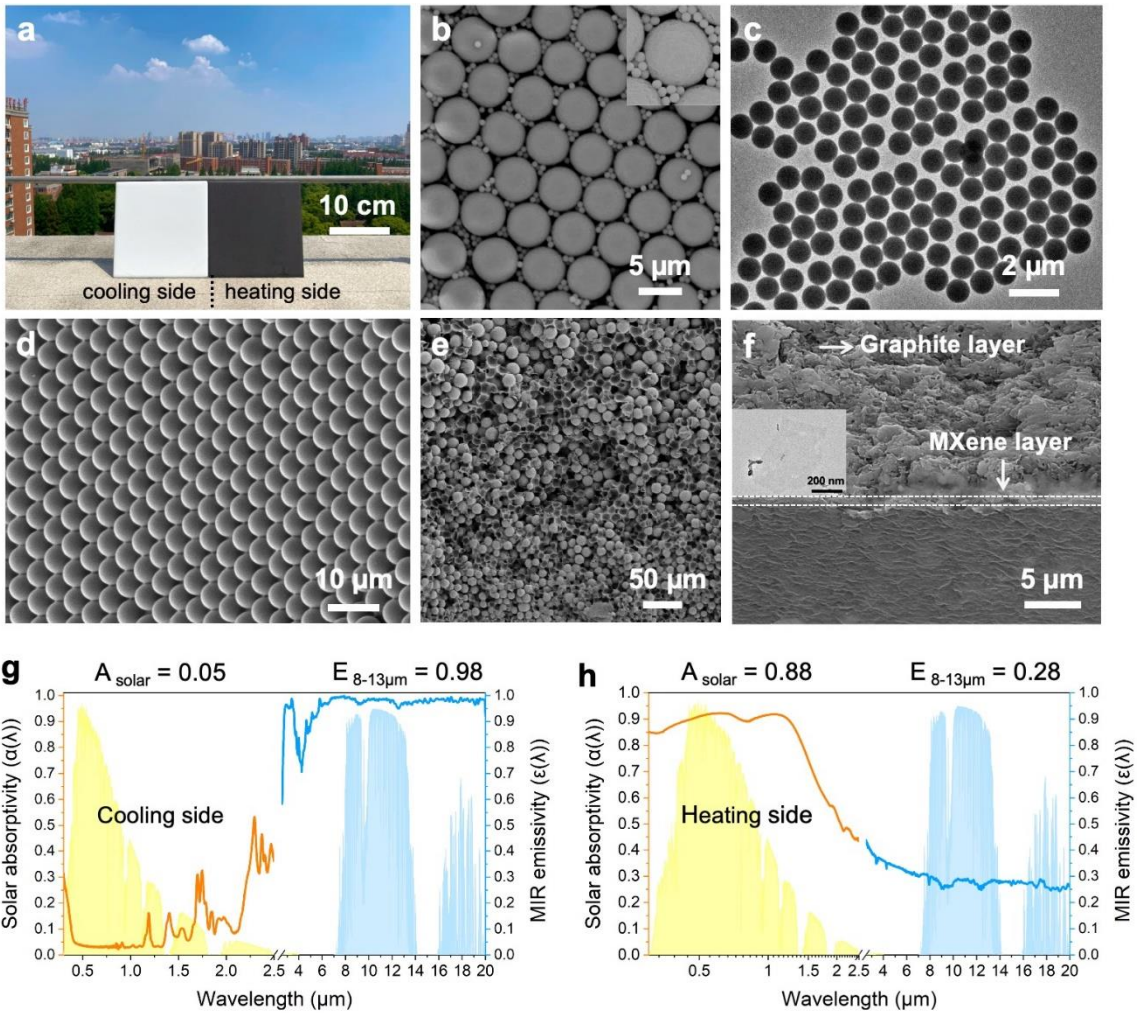


Figure 2. Characterization and spectroscopic response of the trilayer structure. (a) Photographs of the fabricated trilayer structured film with the size of $15 \text{ cm} \times 15 \text{ cm}$ (area = 225 cm^2), indicating the different visible appearance of the cooling and heating sides. (b) SEM micrograph of the binary SiO_2 microsphere structure. (c) TEM micrograph of SiO_2 nanospheres. (d,e) SEM micrographs of hexagonally close-packed SiO_2 monolayer array and PDMS/HGBs composites. (f) SEM micrograph of the G/MXene structure on the heating side (inset, TEM micrograph of the monolayer MXene). (g,h) Solar absorptivity and MIR emissivity spectra of the trilayer structured film.

Further, we experimentally and theoretically investigate the influence of binary SiO_2 microsphere top-layer on the spectroscopic response. As shown in **Figures 3a-b**, the PDMS/HGBs (A), PDMS/HGBs+m- SiO_2 (B) and PDMS/HGBs+m/n- SiO_2 (C) films possess

negligible variations in solar absorptivity due to the high-efficiency scattering effect of abundant HGBs. Intriguingly, the emissivity of C film increases to 0.98 in the range of 8-13 μm compared with A film ($E_{8-13\mu\text{m}} = 0.94$) and B film ($E_{8-13\mu\text{m}} = 0.96$). We attribute this increase in MIR emissivity, particularly in 8-13 μm wavelength, to the structure and intrinsic characteristic of the SiO_2 microsphere array combined with SiO_2 nanospheres. First, the binary SiO_2 microsphere is conducive to increasing specific surface area and the probability of infrared absorption/emission through multiple diffuse reflections at various incident angles.²² Second, it is observed in Figure 3c that the multiple extinction peaks at the 7.9, 9.3 and 12.5 μm of PDMS and the phonon-polariton resonances at 9.7 μm of SiO_2 enable to eject packets of infrared emission across the atmospheric transparency window. Third, as evident from Figure 3d, the medium behavior of the micro-and nanoscale SiO_2 phase reduces the effective refractive index and leads to a more gradual refractive index transition to improve impedance match across the PDMS-air boundary in the LWIR wavelengths, which reduces the surface reflectance and increases air-medium interface absorption at MIR regions.²⁰ In addition, the finite-difference time-domain (FDTD) simulations are performed to reveal that multiple Mie resonances of n- SiO_2 and m- SiO_2 can be excited to control the thermal emission dispersion in the infrared wavelength (Figure 3e). The electric field profiles of PDMS, PDMS+m- SiO_2 and PDMS+m/n- SiO_2 at 2.93 μm , 8.94 μm , 10.83 μm and 12.65 μm further confirm the resonance absorption follows a strong dependence on the micro-and nanoscale SiO_2 , in good qualitative agreement with experimental measurements (Figures 3f, S3 and S4). As expected, the C film demonstrates slightly higher net heating power comparing with A and B films, as shown in Figure S5.

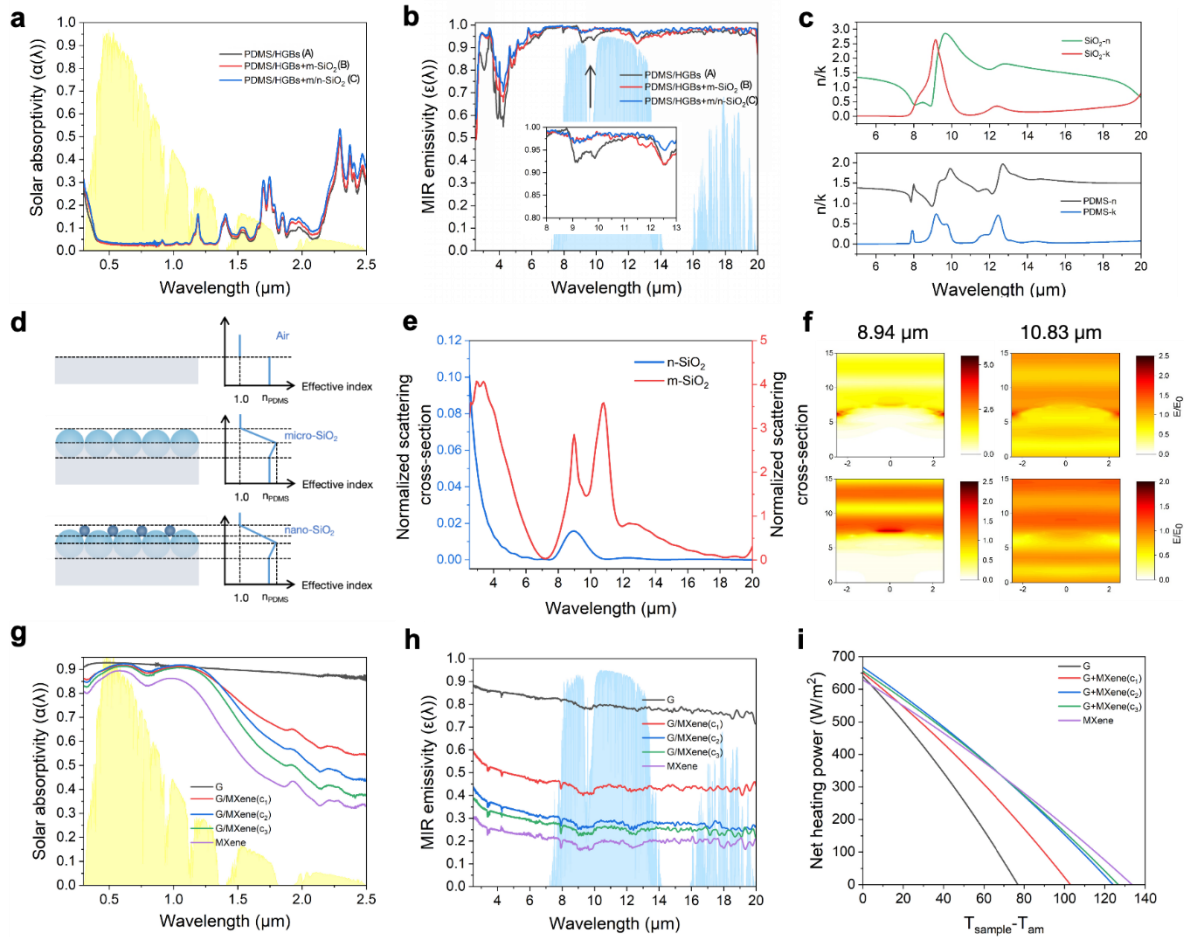


Figure 3. Optical performance optimization of the trilayer structure. (a,b) Solar absorptivity and MIR emissivity spectra of the A, B and C films, respectively. (c) Spectral refractive index (n) and extinction coefficient (κ) of the SiO_2 and PDMS. (d) Schematic diagram of the variations of refractive index with the flat PDMS surface, PDMS/ SiO_2 microsphere surface and PDMS/ SiO_2 micro-nano sphere surface. (e) Simulated normalized scattering cross-section of the 700 nm n- SiO_2 and 5 μm m- SiO_2 . (f) Electric field profiles of the PDMS+m- SiO_2 (left) and PDMS+m/n- SiO_2 (right) at 8.94 μm and 10.83 μm , separately. (g-i) Variations in the solar absorptivity spectra, MIR emissivity spectra and net heating power of the G/MXene composite film with MXene concentration, respectively.

As aforementioned, ideal heating mode is expected to have a high solar absorptivity and low MIR emissivity. The graphite as a classic solar absorbent ($A_{\text{solar}} = 0.92$) is versatile for the creation of solar heating coatings, however, the MIR emissivity of graphite is higher than 0.80

owing to the crystal structure and carbon atoms (Figures 3g-h). The visible black but infrared white nonmetallic materials are highly desired, which have been a long-standing challenge for decades.^{49, 50} The 2D transition metal carbide material, Ti₃C₂ MXene nanochip, has a MIR emissivity as low as 0.19 and shows great potential in radiative heating (Figure 3h).⁵¹ However, the blackbody-like Ti₃C₂ MXene is not an ideal solar absorber, thus we construct a graphite inner layer and MXene functionalized outer layer *via* a simple coating method. Apparently, the solar absorptivity of the obtained G/MXene composite film drops from 0.92 to 0.81 and the MIR emissivity drops from 0.80 to 0.19 in a nearly linear relationship with the increase of MXene concentration (Figures 3g-h). How to integrate the “trade-off” between low MIR emissivity and high solar absorptivity? We therewith compare the net heating power as a function of the temperature difference based on the experimental measured solar and MIR spectra (Figure 3i). Consequently, the experimentally optimized G/MXene (c₂) composite film demonstrates the highest net heating power, making it attractive for practical energy-saving use.

Subambient cooling and above-ambient heating performance of the trilayer structure.

We conduct the subambient cooling and above-ambient heating measurements on a flat roof of an eleven-story building under a clear sky in Shanghai, China (31° 18' 22" N, 121° 30' 17" E). For a more intuitive analysis, two different cooling test apparatuses are schematically shown in Figure S6. One is covered with a 10-μm-thick transparent PE as a wind shield and the other is directly open to the sky without any type of cover. Promisingly, for the first experimental apparatus, the high R_{solar} and E_{8-13μm} allow our cooling-mode asymmetric structured film to

achieve remarkable daytime subambient cooling of 9.8 °C under solar irradiance of 835 W/m², wind speed of 0.12 m/s and relative humidity of 56 % (**Figures 4a, b and S7a**). When using the other experimental apparatus, a lower temperature reduction of 6.8 °C are obtained under a solar irradiance of 682 W/m², wind speed of 0.07 m/s and relative humidity of 44 % due to the inevitable thermal convection effect (Figure S8). To further elucidate the radiative cooling performance of our cooling-mode asymmetric structured film, we calculate the cooling power as a function of the temperature reduction based on the experimental measured solar and MIR spectra, demonstrating a net cooling power of 76.6 W/m² (Figure 4c). More exhilaratingly, we can see a distinct temperature difference of more than 10 °C between the cooling-mode asymmetric structured film and surroundings from the IR image measured under direct sunlight (Figure 4d).

Parallel with the previous method, an above-ambient heating measurement of the heating-mode asymmetric structured film is carried out in winter. As shown in Figures 4e, f and S7b, the high A_{solar} and low $E_{8-13\mu\text{m}}$ allow our heating-mode asymmetric structured film to achieve distinct daytime above-ambient heating of 16.3 °C under a solar irradiance of 605 W/m², wind speed of 0.08 m/s and relative humidity of 19 % with a theoretical net heating power of 667.8 W/m² (Figure 4g). An above-ambient heating of 12.9 °C under a solar irradiance of 663 W/m², wind speed of 0.05 m/s and relative humidity of 39 % can also be observed in Figure S9. Likewise, the IR image of the heating-mode asymmetric structured film has a substantial temperature increase of ~10 °C compared with surroundings and more than ~15 °C compared with cooling-mode film (Figure 4h). Additionally, the potential of personal thermal management application can be imagined by attaching a piece of the trilayer structured film to

the volunteer's fabric (Figure S10).

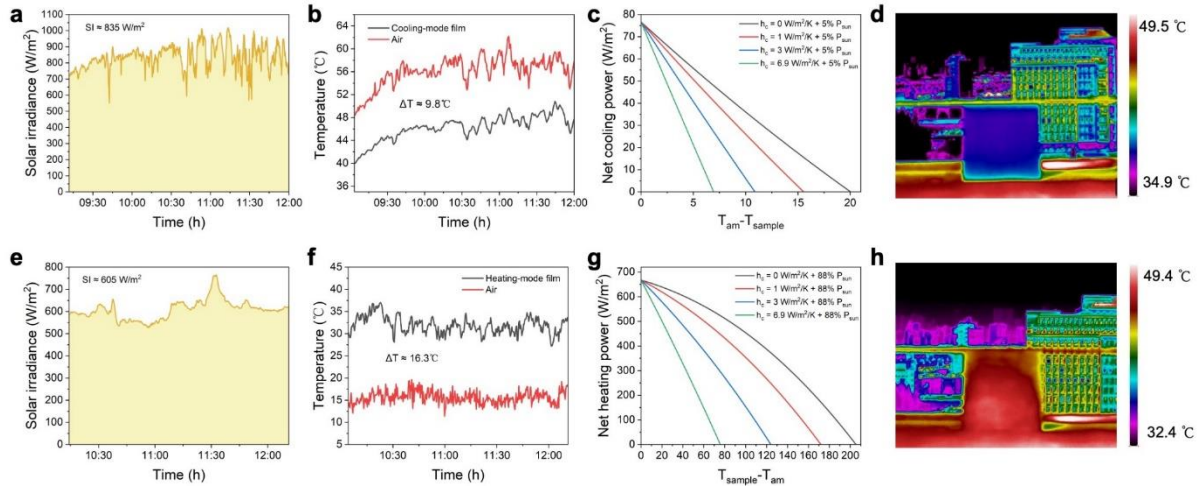


Figure 4. Outdoor real-time cooling and heating tests of the trilayer structured film on the rooftop at the University of Shanghai for Science and Technology under a clear sky on and June 15 and December 25, 2023, respectively. (a,b) Measured solar irradiance and the temperatures of air and cooling-mode asymmetric structured film. (c) Calculated net cooling power of cooling-mode asymmetric structured film during the daytime. Heat transfer coefficient values of 0, 1, 3, and 6.9 $\text{W}/(\text{m}^2 \text{ K})$ are used in the calculations. (d) IR image of the cooling-mode asymmetric structured film. (e,f) Measured solar irradiance and the temperatures of air and heating-mode asymmetric structured film. (g) Calculated net heating power of cooling-mode asymmetric structured film during the daytime. h) IR image of the heating-mode asymmetric structured film.

Practicability and energy saving potential. To improve the durability in various atmospheric humidity conditions, both the cooling side and heating side of the asymmetric structured film is modified with 1H,1H,2H,2H-perfluorooctyltrichlorosilane (PFOTS) by chemical vapor deposition (CVD) method. For the cooling side, It is interesting to note that the WCAs of A, B and C films are all increased after surface fluorosilane treatment, but only the C film (cooling-side of asymmetric structured film) reaches a superhydrophobic state with an apparent WCA of 156° (Figure 5a), indicating its capability to block rain and moisture which

is one of the most important features for building envelop coatings. The combination of enrichment of abundant C-F bonds on the surfaces and the micro-and nanoscale SiO₂ roughness decouples the surface wettability from the bulk properties of the PDMS/HGBs and endows a robust superhydrophobic performance^{52, 53}. More importantly, as shown in the schematic wetting model analysis in Figure 5b, with a further increase of hierarchy and roughness, the micro-and nanoscale structure prevents air stored in the gaps from being expelled by droplet and results in the reduction in the contact area of the solid surface as well as the adhesion force of droplet. Thus, the droplet on the surface clumps gradually to a sphere and transfers from Wenzel to Cassie-Baxter wetting model. When we introduce a water droplet containing red dye on the surface of C film, the droplet automatically slides down without any residuals (Figure 5c), showing typical self-cleaning property. Even after accelerated weathering treatment for 480 h (each accelerated weathering test cycle including the UV irradiation at 310 nm wavelength with intensity of 0.71 W/m² at 60 °C for 4 h, followed by condensation at 50 °C for 4 h with UV lamps off), the C film presents no blistering, peeling, cracking or color changing, and exhibits slight fluctuations and negligible variations (Figure 5d). For the heating side, the hydrophobicity of the G/MXene composite film shows a certain improvement form WCA of 115° to WCA of 125° (Figure S11) after surface modification using fluorosilane, which is less than the cooling side due to the relatively flat surface structure. Besides, our trilayer structured film exhibit good tensile performance with a breakage strength of 1.46 Mpa compared with PDMS of 1.2 Mpa (Figure S12). After various deformations for several hundred times, the trilayer structured film can completely recover to its original configuration without cracks or bends, showing its good mechanical stability and flexibility (Figure S13 and Movie

1).

The trilayer structured film is superior to single-cooling or single-heating films, which can realize all-season on-demand thermal management according to actual climate changes by switching the working mode. We use EnergyPlus to calculate the annual energy savings of the trilayer structured film as the commercial and residential roof coating to quantitatively predict the potential annual energy consumption in ten cities representing different dividing regions of the world (London, Harbin, Rome, Beijing, Washington D.C., Shanghai, Lhasa, Cape Town, Buenos Aires, Canberra) (Figures 5e, f and S14). It can be noticed that our trilayer structured film has a significant advantage and can save up to 12.04% and 6.67% of annual residential cooling and heating energy consumption, respectively, compared with commercially available white paint. Furthermore, single-cooling and single-heating modes can only achieve limited energy savings and even increase energy consumption owing to the overcooling and overheating effects. The predicted average annual electricity saving of the trilayer structured film shows 391.4 mW·h for cooling and 1232.2 mW·h for heating. These energy savings correspond to a global CO₂ emission reduction is estimated to be 0.32 and 1.02 million kg for cooling and heating, respectively (Figure 5g). Besides, Figure 5h shows the map of global energy-saving potential of trilayer structured film compared with commercial white paint, demonstrating the potential for building energy conservation in midlatitude regions.

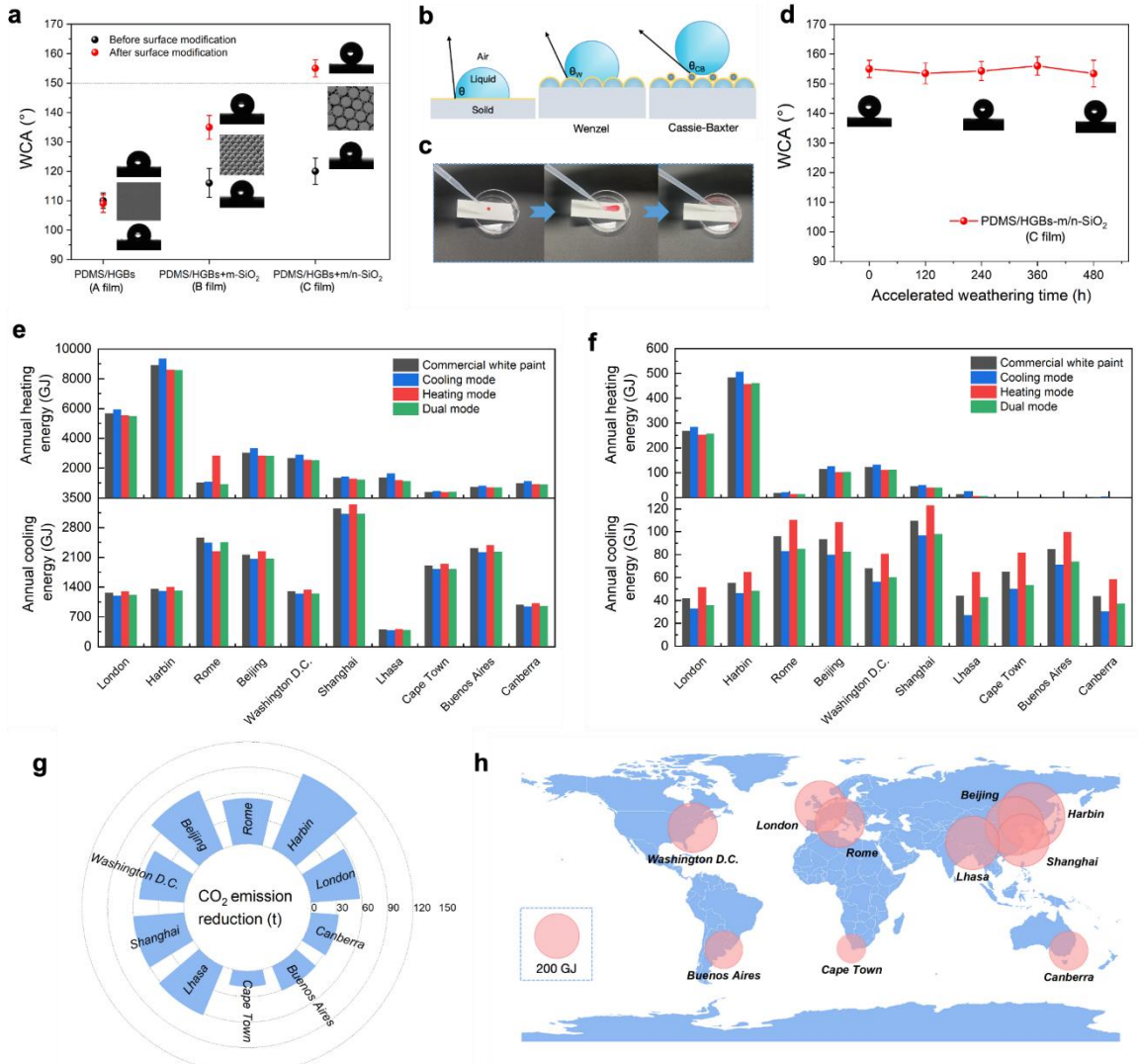


Figure 5. Superhydrophobicity, durability and modeled full-year building energy savings for the trilayer structured film. (a) WCA variations of A, B and C films after surface modification using fluorosilane. (b) A schematic wetting model analysis of A, B and C films. The bright yellow area represents fluorosilane. (c) Dust self-cleaning test of the C film. (d) WCA variations of the C film with the accelerated weathering time. (e,f) Energy consumption of commercial and residential buildings in ten typical cities, respectively. (g) Predicted annual global CO₂ emission reduction for the modeled buildings in ten typical cities. (h) Map of global energy-saving potential compared with commercial white paint.

CONCLUSION

In conclusion, we demonstrate the trilayer structure composed of a binary micro-nano SiO₂

top-layer, a PDMS/HGBs interlayer and a graphite/Ti₃C₂ MXene nanochip underlayer for all-season radiative thermoregulation. The cooling-mode asymmetric structured film achieves a R_{solar} of 0.95 and an E_{8-13μm} of 0.98, endowing a comparable daytime subambient cooling of 9.8 °C with a theoretical net cooling power of 76.6 W/m². Likewise, the heating-mode film realizes an A_{solar} of 0.88 and an E_{8-13μm} of 0.28, yielding a daytime above-ambient heating of 16.3 °C with a theoretical net heating power of 667.8 W/m². Promisingly, the visible and infrared spectra regulation amplitude ($\eta_R = 7.92$, $\eta_E = 3.5$), superb radiative thermoregulation capability ($\Delta T_{cooling-heating} = 26.1$ °C), superhydrophobicity (WCA = 156 °) and environmental durability provide our trilayer structured film great potential in building thermoregulation. Moreover, in contrast to commercial white paint, the trilayer structured film can save up to 12.04% and 6.67% of annual residential cooling and heating energy consumption, respectively, which has a significant advantage over single-cooling and single-heating modes in electricity savings and global CO₂ emission reduction.

ASSOCIATED CONTENT

Supporting Information

Supporting Information associated with this article can be found in the online version.

Materials; fabrication of dual-mode asymmetric structured film; characterizations; calculations of average solar reflectivity and MIR emissivity; FDTD simulations; outdoor real-time radiative cooling and heating measurements; theoretical model of the radiative cooling and heating performance; energy-saving analysis of using EnergyPlus software; SEM micrograph of hexagonally close-packed SiO₂ monolayer array; SEM micrographs of HGBs and Energy-

dispersive X-ray spectroscopy elemental mappings of C, Si, O, K, B, Na, and Ca in the PDMS/HGBs interlayer; electric field profiles of PDMS at 8.94 μm and 10.83 μm ; electric field profiles of the PDMS, PDMS+m-SiO₂ and PDMS+m/n-SiO₂ at 2.93 μm and 12.65 μm , separately; schematic of the setup for cooling testing performance under sunlight; wind speed and relative humidity for outdoor real-time cooling and heating tests, respectively; measured wind speed, relative humidity, solar irradiance, air temperature and cooling-mode asymmetric structured film temperature on October 23, 2023; measured wind speed, relative humidity, solar irradiance, air temperature and cooling-mode asymmetric structured film temperature on November 21, 2023; IR images of the volunteer wearing a piece of dual-mode asymmetric structured film under direct sunlight; mechanical strength tests of the PDMS and asymmetric structured film versus elongation; commercial and residential building models and roof structure used in EnergyPlus; comparison of optic performances of the dual-mode cooling and heating films.

AUTHOR INFORMATION

Corresponding Author

Yinan Zhang – *School of Artificial Intelligence Science and Technology, University of Shanghai for Science and Technology, Shanghai 200093, China. Institute of Photonic Chips, University of Shanghai for Science and Technology, Shanghai 200093, China; Email: zhangyinan@usst.edu.cn*

Min Gu – *School of Artificial Intelligence Science and Technology, University of Shanghai for Science and Technology, Shanghai 200093, China. Institute of Photonic Chips,*

*University of Shanghai for Science and Technology, Shanghai 200093, China; Email:
gumin@usst.edu.cn (M.Gu)*

Authors

Tong Wang – *School of Artificial Intelligence Science and Technology, University of Shanghai for Science and Technology, Shanghai 200093, China. Institute of Photonic Chips, University of Shanghai for Science and Technology, Shanghai 200093, China*

Shuqi Zhang – *School of Artificial Intelligence Science and Technology, University of Shanghai for Science and Technology, Shanghai 200093, China. Institute of Photonic Chips, University of Shanghai for Science and Technology, Shanghai 200093, China*

Qian Zhu – *School of Artificial Intelligence Science and Technology, University of Shanghai for Science and Technology, Shanghai 200093, China. Institute of Photonic Chips, University of Shanghai for Science and Technology, Shanghai 200093, China*

Jie Zhang – *School of Artificial Intelligence Science and Technology, University of Shanghai for Science and Technology, Shanghai 200093, China. Institute of Photonic Chips, University of Shanghai for Science and Technology, Shanghai 200093, China*

Yu Zhang – *Department of Materials Science and State Key Laboratory of Molecular Engineering of Polymers, Fudan University, Shanghai 200433, China*

Yanping Du – *School of Engineering, Lancaster University, Lancaster LA1 4YW, UK*

Limin Wu – *Department of Materials Science and State Key Laboratory of Molecular Engineering of Polymers, Fudan University, Shanghai 200433, China*

Funding

Y.Z. acknowledges the support by the National Natural Science Foundation of China (NSFC) (Grant No. 62175154), the Shanghai Pujiang Program (20PJ1411900), the Shanghai Science

and Technology Program (21ZR1445500) and the Program for Professor of Special Appointment (Eastern Scholar) at Shanghai Institutions of Higher Learning. T.W. acknowledges the support by the National Natural Science Foundation of China (NSFC) (Grant No. 52303091) and the Shanghai Yangfan Program (22YF1430200). J. Z. acknowledges the Sponsored by Shanghai Pujiang Program (23PJ1409700).

Notes

The authors declare no competing financial interest.

REFERENCES

- (1) Radiant cooling systems market.
<https://www.transparencymarketresearch.com/radiant-cooling-systems-market.html>.
- (2) Lyu, W.; Li, X.; Shi, W.; Wang, B.; Huang, X. A general method to evaluate the applicability of natural energy for building cooling and heating: Revised degree hours. *Energ. Buildings* **2021**, *250*, 111277.
- (3) Sherwood, S. C. Adapting to the challenges of warming. *Science* **2020**, *370* (6518), 782-783.
- (4) Ürge-Vorsatz, D.; Cabeza, L. F.; Serrano, S.; Barreneche, C.; Petrichenko, K. Heating and cooling energy trends and drivers in buildings. *Renewable Sustainable Energy Rev.* **2015**, *41*, 85-98.
- (5) Chen, Z.; Zhu, L.; Li, W.; Fan, S. Simultaneously and synergistically harvest energy from the sun and outer space. *Joule* **2019**, *3* (1), 101-110.
- (6) Munday, J. N. Tackling climate change through radiative cooling. *Joule* **2019**, *3* (9), 2057-2060.
- (7) Zhao, D.; Tang, H. Staying stably cool in the sunlight. *Science* **2023**, *382* (6671), 644-645.
- (8) Yin, X.; Yang, R.; Tan, G.; Fan, S. Terrestrial radiative cooling: Using the cold universe as a renewable and sustainable energy source. *Science* **2020**, *370* (6518), 786-791.
- (9) Lim, X. The super-cool materials that send heat to space. *Nature* **2020**, *577* (7788), 18-21.
- (10) Fan, S.; Li, W. Photonics and thermodynamics concepts in radiative cooling. *Nat. Photonics* **2022**, *16*, 182-190..
- (11) Rephaeli, E.; Raman, A.; Fan, S. Ultrabroadband photonic structures to achieve high-performance daytime radiative cooling. *Nano Lett* **2013**, *13* (4), 1457-1461.

- (12) Raman, A. P.; Anoma, M. A.; Zhu, L.; Rephaeli, E.; Fan, S. Passive radiative cooling below ambient air temperature under direct sunlight. *Nature* **2014**, *515* (7528), 540-544.
- (13) Wu, D.; Liu, C.; Xu, Z.; Liu, Y.; Yu, Z.; Yu, L.; Chen, L.; Li, R.; Ma, R.; Ye, H. The design of ultra-broadband selective near-perfect absorber based on photonic structures to achieve near-ideal daytime radiative cooling. *Mater. Des.* **2018**, *139*, 104-111.
- (14) Mu, E.; Wu, Z.; Wu, Z.; Chen, X.; Liu, Y.; Fu, X.; Hu, Z. A novel self-powering ultrathin TEG device based on micro/nano emitter for radiative cooling. *Nano Energy* **2019**, *55*, 494-500.
- (15) Zhang, Y.; Chen, Y.; Wang, T.; Zhu, Q.; Gu, M. Ultrahigh performance passive radiative cooling by hybrid polar dielectric metasurface thermal emitters. *Opto-Electronic Advances* **2024**, *7* (4), 230194-230191-230194-230199.
- (16) Zhai, Y.; Ma, Y.; David, S. N.; Zhao, D.; Lou, R.; Tan, G.; Yang, R.; Yin, X. Scalable-manufactured randomized glass-polymer hybrid metamaterial for daytime radiative cooling. *Science* **2017**, *355* (6329), 1062-1066.
- (17) Hossain, M. M.; Jia, B.; Gu, M. A metamaterial emitter for highly efficient radiative cooling. *Adv. Opt. Mater.* **2015**, *3* (8), 1047-1051.
- (18) Zeng, S.; Pian, S.; Su, M.; Wang, Z.; Wu, M.; Liu, X.; Chen, M.; Xiang, Y.; Wu, J.; Zhang, M. Hierarchical-morphology metafabric for scalable passive daytime radiative cooling. *Science* **2021**, *373* (6555), 692-696.
- (19) Lin, K.-T.; Nian, X.; Li, K.; Han, J.; Zheng, N.; Lu, X.; Guo, C.; Lin, H.; Jia, B. Highly efficient flexible structured metasurface by roll-to-roll printing for diurnal radiative cooling. *eLight* **2023**, *3* (1), 22.
- (20) Mandal, J.; Fu, Y.; Overvig, A. C.; Jia, M.; Sun, K.; Shi, N. N.; Zhou, H.; Xiao, X.; Yu, N.; Yang, Y. Hierarchically porous polymer coatings for highly efficient passive daytime radiative cooling. *Science* **2018**, *362* (6412), 315-319.
- (21) Li, D.; Liu, X.; Li, W.; Lin, Z.; Zhu, B.; Li, Z.; Li, J.; Li, B.; Fan, S.; Xie, J. Scalable and hierarchically designed polymer film as a selective thermal emitter for high-performance all-day radiative cooling. *Nat. Nanotechnol.* **2020**, *16* (2), 153-158.
- (22) Wang, T.; Wu, Y.; Shi, L.; Hu, X.; Chen, M.; Wu, L. A structural polymer for highly efficient all-day passive radiative cooling. *Nat. Commun.* **2021**, *12* (1), 365.
- (23) Li, T.; Zhai, Y.; He, S.; Gan, W.; Wei, Z.; Heidarnejad, M.; Dalgo, D.; Mi, R.; Zhao, X.; Song, J.; et al. A radiative cooling structural material. *Science* **2019**, *364* (6442), 760-763.

- (24) Zhao, X.; Li, T.; Xie, H.; Liu, H.; Wang, L.; Qu, Y.; Li, S. C.; Liu, S.; Brozena, A. H.; Yu, Z. A solution-processed radiative cooling glass. *Science* **2023**, *382* (6671), 684-691.
- (25) Zhang, Y.; Wang, T.; Mei, X.; Chen, M.; Wu, L. Ordered Porous Polymer Films for Highly Efficient Passive Daytime Radiative Cooling. *Acs Photonics* **2023**, *10* (9), 3124-3132.
- (26) Wang, T.; Wu, X.; Zhu, Q.; Chen, Y.; Zhang, S.; Gu, M.; Zhang, Y. A scalable and durable polydimethylsiloxane-coated nanoporous polyethylene textile for daytime radiative cooling. *Nanophotonics* **2024**, *13*(5): 601-609.
- (27) Gentle, A. R.; Smith, G. B. A Subambient Open Roof Surface under the Mid-Summer Sun. *Adv. Sci.* **2015**, *2* (9), 1500119.
- (28) Aili, A.; Wei, Z. Y.; Chen, Y. Z.; Zhao, D. L.; Yang, R. G.; Yin, X. B. Selection of polymers with functional groups for daytime radiative cooling. *Mater. Today Phys.* **2019**, *10*.
- (29) Zhou, L.; Song, H.; Liang, J.; Singer, M.; Zhou, M.; Stegenburgs, E.; Zhang, N.; Xu, C.; Ng, T.; Yu, Z.; et al. A polydimethylsiloxane-coated metal structure for all-day radiative cooling. *Nat. Sustain.* **2019**, *2* (8), 718-724.
- (30) Zhang, H.; Ly, K. C. S.; Liu, X.; Chen, Z.; Yan, M.; Wu, Z.; Wang, X.; Zheng, Y.; Zhou, H.; Fan, T. Biologically inspired flexible photonic films for efficient passive radiative cooling. *Proc. Natl. Acad. Sci. U.S.A.* **2020**, *117* (26), 14657-14666.
- (31) Liu, X.; Xiao, C.; Wang, P.; Yan, M.; Wang, H.; Xie, P.; Liu, G.; Zhou, H.; Zhang, D.; Fan, T. Biomimetic photonic multiform composite for high-performance radiative cooling. *Adv. Opt. Mater.* **2021**, 2101151.
- (32) Lin, K.; Chen, S.; Zeng, Y.; Ho, T. C.; Zhu, Y.; Wang, X.; Liu, F.; Huang, B.; Chao, C. Y.-H.; Wang, Z. Hierarchically structured passive radiative cooling ceramic with high solar reflectivity. *Science* **2023**, *382* (6671), 691-697.
- (33) Li, X.; Peoples, J.; Huang, Z.; Zhao, Z.; Qiu, J.; Ruan, X. Full daytime sub-ambient radiative cooling in commercial-like paints with high figure of merit. *Cell Rep. Phys. Sci.* **2020**, *1* (10), 100221.
- (34) Mandal, J.; Yang, Y.; Yu, N.; Raman, A. P. Paints as a scalable and effective radiative cooling technology for buildings. *Joule* **2020**, *4* (7), 1350-1356.
- (35) Huang, W.; Chen, Y.; Luo, Y.; Mandal, J.; Li, W.; Chen, M.; Tsai, C. C.; Shan, Z.; Yu, N.; Yang, Y. Scalable Aqueous Processing-Based Passive Daytime Radiative Cooling Coatings. *Adv. Funct. Mater.* **2021**, *31* (19), 2010334.
- (36) Tang, K.; Dong, K.; Li, J.; Gordon, M. P.; Reichertz, F. G.; Kim, H.; Rho, Y.; Wang, Q.; Lin, C.-Y.;

Grigoropoulos, C. P. Temperature-adaptive radiative coating for all-season household thermal regulation. *Science* **2021**, *374* (6574), 1504-1509.

(37) Wang, T.; Zhang, Y.; Chen, M.; Gu, M.; Wu, L. Scalable and waterborne titanium-dioxide-free thermochromic coatings for self-adaptive passive radiative cooling and heating. *Cell Rep. Phys. Sci.* **2022**, *3* (3), 100782.

(38) Zhu, L.; Tian, L.; Jiang, S.; Han, L.; Liang, Y.; Li, Q.; Chen, S. Advances in photothermal regulation strategies: from efficient solar heating to daytime passive cooling. *Chem. Soc. Rev.* **2023**.

(39) Rao, Y.; Dai, J.; Sui, C.; Lai, Y.-T.; Li, Z.; Fang, H.; Li, X.; Li, W.; Hsu, P.-C. Ultra-Wideband Transparent Conductive Electrode for Electrochromic Synergistic Solar and Radiative Heat Management. *ACS Energy Lett.* **2021**, *6* (11), 3906-3915.

(40) Li, J.; Dong, K.; Zhang, T.; Tseng, D.; Fang, C.; Guo, R.; Li, J.; Xu, Y.; Dun, C.; Urban, J. J. Printable, emissivity-adaptive and albedo-optimized covering for year-round energy saving. *Joule* **2023**, *7* (11), 2552-2567.

(41) Dong, Y.; Meng, W.; Wang, F.; Han, H.; Liang, H.; Li, X.; Zou, Y.; Yang, C.; Xu, Z.; Yan, Y. “Warm in Winter and Cool in Summer”: Scalable Biochameleon Inspired Temperature-Adaptive Coating with Easy Preparation and Construction. *Nano Lett.* **2023**, *23* (19), 9034-9041.

(42) Zhang, Q.; Lv, Y.; Wang, Y.; Yu, S.; Li, C.; Ma, R.; Chen, Y. Temperature-dependent dual-mode thermal management device with net zero energy for year-round energy saving. *Nat. Commun.* **2022**, *13* (1), 4874.

(43) Zhang, Q.; Wang, Y.; Lv, Y.; Yu, S.; Ma, R. Bioinspired zero-energy thermal-management device based on visible and infrared thermochromism for all-season energy saving. *Proc. Natl. Acad. Sci.* **2022**, *119* (38), e2207353119.

(44) Mei, X.; Wang, T.; Chen, M.; Wu, L. A self-adaptive film for passive radiative cooling and solar heating regulation. *J. Mater. Chem. A* **2022**, *10* (20), 11092-11100.

(45) Sui, C.; Pu, J.; Chen, T.-H.; Liang, J.; Lai, Y.-T.; Rao, Y.; Wu, R.; Han, Y.; Wang, K.; Li, X. Dynamic electrochromism for all-season radiative thermoregulation. *Nat. Sustain.* **2023**, *6* (4), 428-437.

(46) Gu, B.; Xu, Q.; Wang, H.; Pan, H.; Zhao, D. A Hierarchically Nanofibrous Self-Cleaning Textile for Efficient Personal Thermal Management in Severe Hot and Cold Environments. *ACS Nano* **2023**, *17* (18), 18308-18317.

(47) Xie, A. Q.; Zhu, L.; Liang, Y.; Mao, J.; Liu, Y.; Chen, S. Fiber-spinning Asymmetric Assembly for Janus-structured Bifunctional Nanofiber Films towards All-Weather Smart Textile. *Angew. Chem.* **2022**, *134* (40), e202208592.

(48) Yuan, H.; Liu, R.; Cheng, S.; Li, W.; Ma, M.; Huang, K.; Li, J.; Cheng, Y.; Wang, K.; Yang, Y. Scalable

Fabrication of Dual-Function Fabric for Zero-Energy Thermal Environmental Management through Multiband, Synergistic, and Asymmetric Optical Modulations. *Adv. Mater.* **2023**, 2209897.

(49) Zhang, Y.; Li, L.; Cao, Y.; Yang, Y.; Wang, W.; Wang, J. High-strength, low infrared-emission nonmetallic films for highly efficient Joule/solar heating, electromagnetic interference shielding and thermal camouflage.

Mater. Horiz. **2023**, 10 (1), 235-247.

(50) Li, K.; Lin, C.; Liu, G.; Wang, G.; Ma, W.; Li, M.; Li, Y.; Huang, B. Stepless IR Chromism in Ti₃C₂Tx MXene Tuned by Interlayer Water Molecules. *Adv. Mater.* **2023**, 2308189.

(51) Li, Y.; Xiong, C.; Huang, H.; Peng, X.; Mei, D.; Li, M.; Liu, G.; Wu, M.; Zhao, T.; Huang, B. 2D Ti₃C₂Tx MXenes: visible black but infrared white materials. *Adv. Mater.* **2021**, 33 (41), 2103054.

(52) Ma, M.; Hill, R. M. Superhydrophobic surfaces. *Curr. Opin. Colloid Interface Sci.* **2006**, 11 (4), 193-202.

(53) Roach, P.; Shirtcliffe, N. J.; Newton, M. I. Progress in superhydrophobic surface development. *Soft matter* **2008**, 4 (2), 224-240.

A Trilayer Structure with Surface Binary Microsphere Array for Radiative Cooling and Heating Regulation

Tong Wang,[†] Shuqi Zhang,[†] Qian Zhu, Jie Zhang, Yu Zhang, Yanping Du, Limin Wu, Min Gu,^{*} Yinan Zhang^{*}

